

Supplementary

Revealing the chemical characteristics of Arctic low-level cloud residuals – in-situ observations from a mountain site

5 Yvette Gramlich^{1,2}, Karolina Siegel^{1,2,3}, Sophie Haslett^{1,2}, Gabriel Freitas^{1,2}, Radovan Krejci^{1,2}, Paul Zieger^{1,2}, and Claudia Mohr^{1,2}

¹Department of Environmental Science, Stockholm University, Stockholm, Sweden

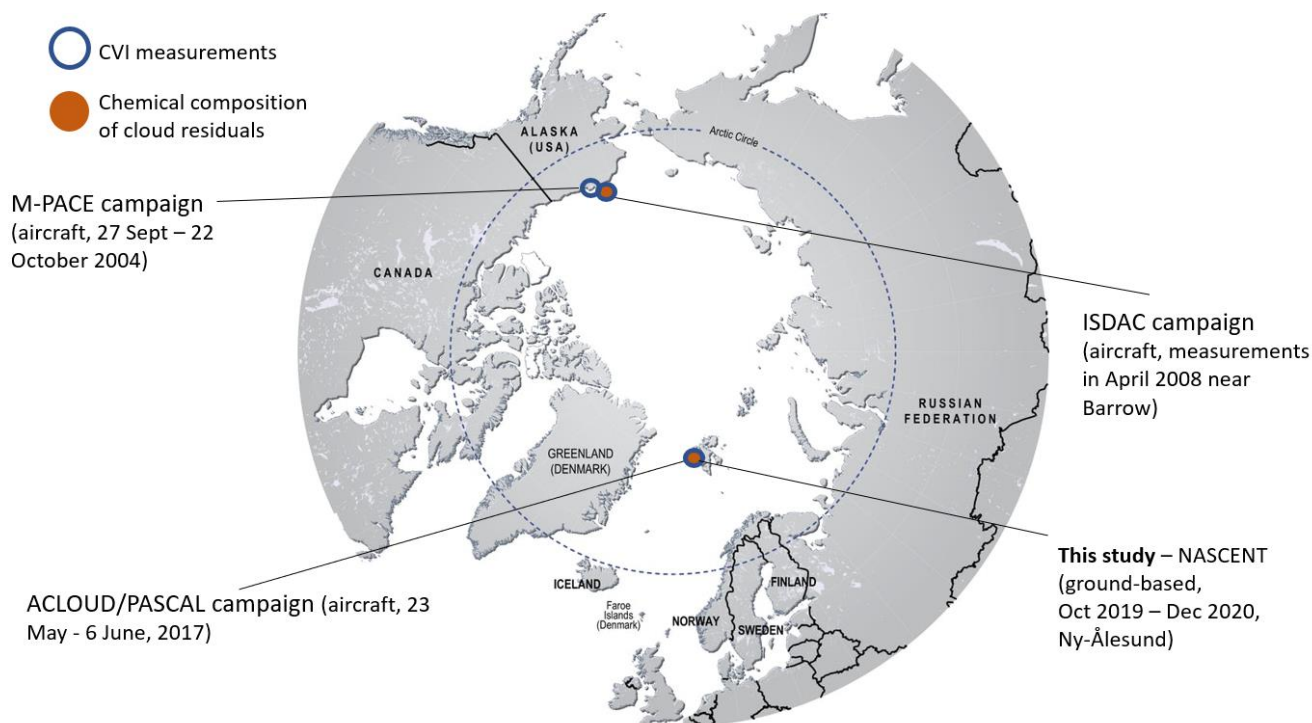
²Bolin Centre for Climate Research, Stockholm University, Stockholm, Sweden

³Department of Meteorology, Stockholm University, Stockholm, Sweden

10

Correspondence to: Claudia Mohr (claudia.mohr@aces.su.se)

S1 Overview of previous studies on the chemical composition of cloud residuals



15

Figure S1: Map of the Arctic showing the sampling location of NASCENT and the locations of previous studies on the chemical composition of Arctic cloud residuals. (Map taken from <https://www.grida.no/resources/8378>.) We note that our cloud residual samples were obtained using a Ground-based Counterflow Virtual Impactor (GCVI), whereas previous cloud residual samples were aircraft based (CVI) (Verlinde et al., 2007; McFarquhar et al., 2011; Wendisch et al., 2019).

S2 Background correction for FIGAERO-CIMS data

The background correction was done following the approach recommended in Cai et al. (2022). We scaled the blank heating signal to the end of the sample signal and subtracted the integrated scaled blank signal from the integrated sample heating (Fig. S2). Since we did not have a blank for each cloud residual sample, we took the blank that was measured closest (with respect to time) to the sample as the respective background (Table S1).

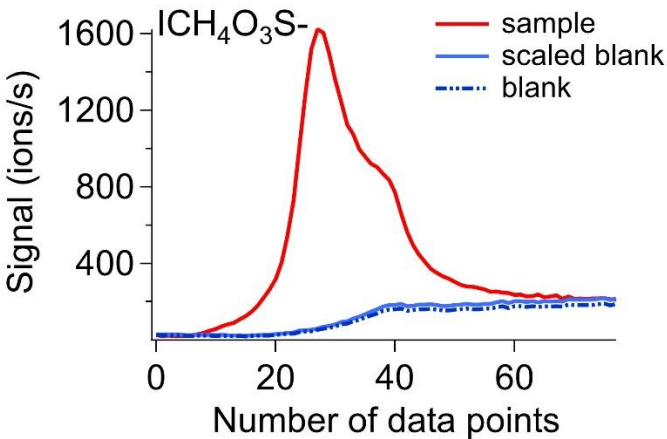


Figure S2: Example of the signal of CH₄O₃S (methanesulfonic acid, MSA) measured as iodide cluster in the cloud residual of Jun 26, 2020, showing how the scaled blank signal was used for background determination. The dashed blue line is the original blank signal and the solid blue line the blank signal scaled to the end of the sample heating. The interval between two data points equals a time period of 30 s.

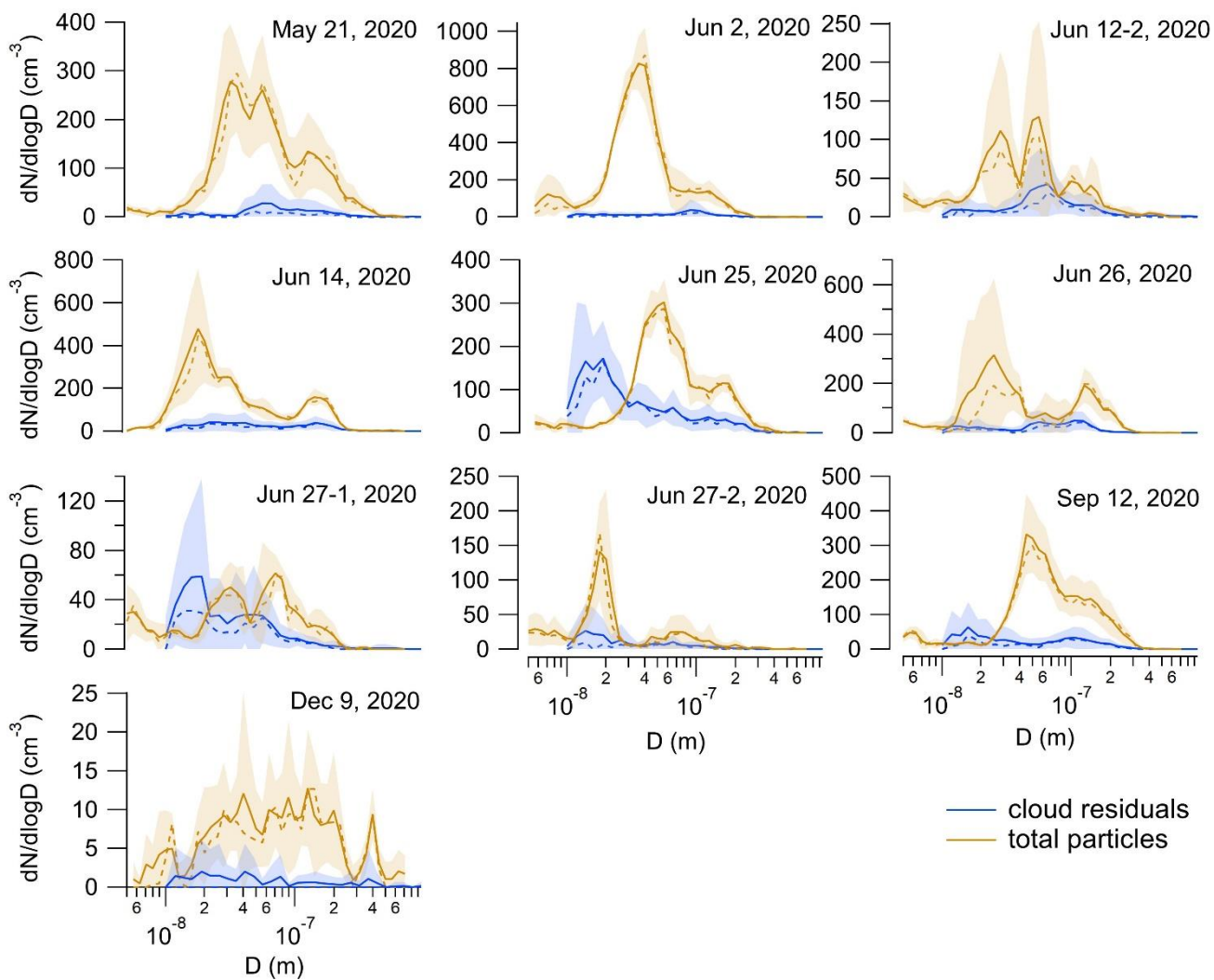
Table S1: Cloud residual samples and the respective blanks used for the background correction. The time in the brackets refers to the respective FIGAERO-CIMS sampling time of the blanks. The sampling times for the cloud residual samples can be found in the main text, Table 1.

Cloud residual sample	Blank used	Cloud residual sample	Blank used
Dec 25, 2019	Jan 19, 2020 (13:05:51-15:36:14)	Jun 25, 2020	Jun 25, 2020 (13:29:00-15:59:09)
May 18, 2020	May 18, 2020 (11:03:03-13:33:05)	Jun 26, 2020	Jun 26, 2020 (10:29:00-12:59:08)
May 21, 2020	May 21, 2020 (16:17:47-18:47:49)	Jun 27-1, 2020	Jun 27, 2020 (07:28:59-09:59:07)
Jun 2, 2020	Jun 12, 2020 (14:50:11-17:20:19)	Jun 27-2, 2020	Jun 27, 2020 (07:28:59-09:59:07)
Jun 12-1, 2020	Jun 12, 2020 (14:50:11-17:20:19)	Sep 12, 2020	Sep 12, 2020 (23:01:39-01:32:00)
Jun 12-2, 2020	Jun 12, 2020 (14:50:11-17:20:19)	Oct 28, 2020	Sep 12, 2020 (23:01:39-01:32:00)
Jun 14, 2020	Jun 13, 2020 (22:20:25- Jun 14 00:50:03)	Dec 9, 2020	Sep 12, 2020 (23:01:39-01:32:00)

S3 Cloud residual size distributions

35 The number size distributions of all cloud residuals not shown in the main text are presented in Figure S3.

During the times when we sampled the cloud residuals on June 25, June 27-1 and September 12, 2020, there was also drizzle present. This can be seen in data from the condensation particle counter (CPC, model 3772, TSI Inc., USA), as well as in the Cloudnet target classification (Fig. S4). The drizzle droplets can splash when they hit the funnel of the wind tunnel of the
40 GCVI and produce several, smaller droplets. This can then be seen as a spike in the total particle number concentration of the CPC measured at a time resolution of 1 s (N_{tot} 1s). This concentration can be compared to the particle number concentration measured with another CPC (model 3772, TSI Inc., USA) behind the differential mobility analyser (DMA, medium Vienna-type, length 0.28 m, outer radius 0.033 m, inner radius 0.025 m) and integrated over the entire size range (N_{int} , time resolution 7 min) by averaging it to the same time resolution (N_{tot} mean). If the size selected by the DMA (D_{scan}) is in the size range of
45 the Aitken mode particles when droplet splashing occurs, the integrated number concentration (N_{int}) will be much higher than N_{tot} mean for the same time interval. Additionally, a large number of Aitken mode particles can be observed in the number size distribution. Therefore, we removed the datapoints for the number size distributions where the median ratio of $N_{\text{int}}/N_{\text{tot}}$ over the entire 2.5 h sampling time was larger than a certain threshold. Fig. S6 shows an example (from September 12, 2020) of how drizzle splashing can be observed in the Differential Mobility Particle Sizer (DMPS) data. The median ratios, the
50 selected threshold and the corresponding number of datapoints that are removed are shown in Table S2.



55 **Figure S3: Average number size distributions of the cloud residuals and the total particles during the corresponding 2.5 h FIGAERO-CIMS sampling time of all remaining samples not shown in the main text. The shaded area represents the standard deviation.**

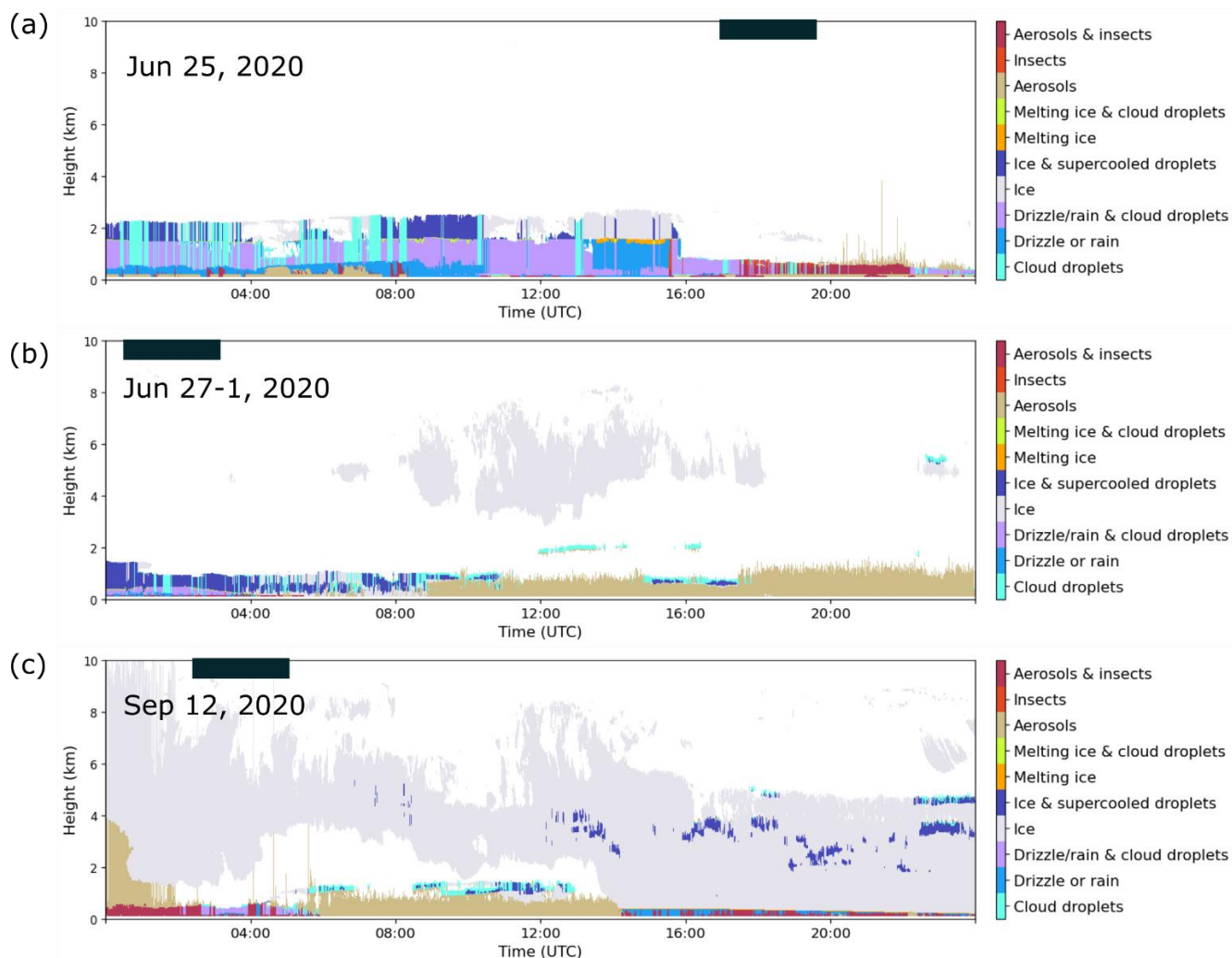


Figure S4: Cloudnet target classification (modified by adding the respective cloud residual sample date, and indicating the approximate sampling times of the cloud with a black bar on top of each subfigure) for (a) June 25, 2020 (Cloudnet (2021), last access: 2022-11-24, 15:35 UTC), (b) June 27-2, 2020 (Cloudnet (2021b), last access: 2022-11-24, 15:28 UTC), (c) September 12, 2020 (Cloudnet (2021a), last access: 2022-11-24, 15:38 UTC), indicating that there was drizzle present during the sampling times of the cloud residuals.

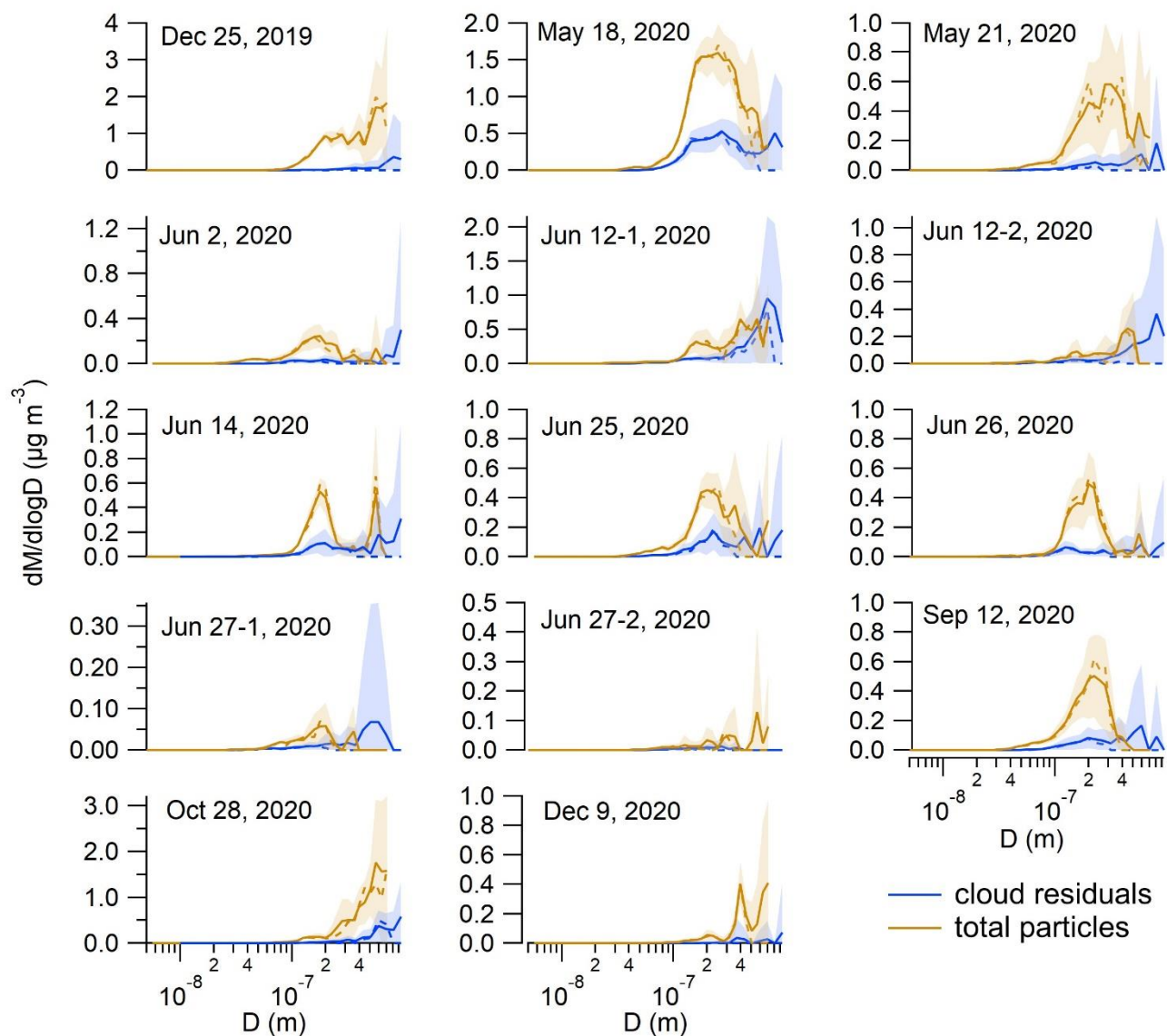


Figure S5: Average mass size distributions of all the cloud residual samples and the total particle population. The shaded area indicates the standard deviation. For the conversion from number to mass a density of 1.3 g cm^{-3} was used, representing secondary organic aerosol (e.g. Alfarrar et al., 2006; Malloy et al., 2009).

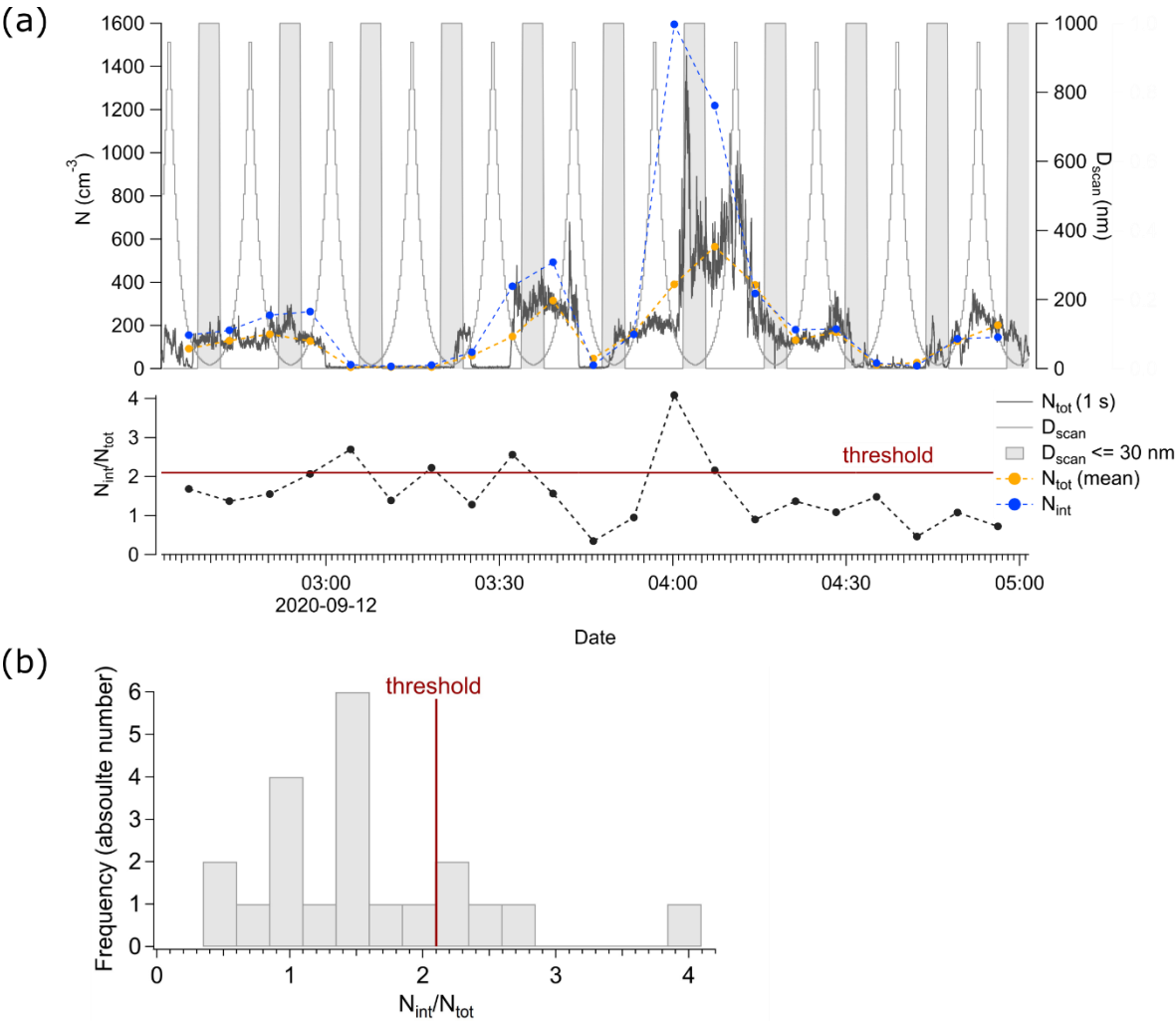


Figure S6: (a) DMPS data from the cloud residual sample of September 12, 2020, as an example of how the droplet splashing of drizzle droplets can be seen as spikes in the N_{tot} (1 s) time series. $D_{scan} \leq 30$ indicates the time periods when the size selected by the DMA was in the small size range, selecting particles up to diameters of 30 nm. The lower panel shows the ratio of N_{int}/N_{tot} and the location of the threshold. **(b)** Histogram of the ratio N_{tot}/N_{int} indicating the location of the selected threshold for filtering the data. For the ratio N_{tot}/N_{int} we took N_{tot} (mean).

Table S2: Cloud case, median ratio of N_{int}/N_{tot} , selected threshold above which the datapoints were removed, and the corresponding number of datapoints that are removed ($Num_{removed}$) from the total number of datapoints (Num_{total}).

Cloud case	Median ratio N_{int}/N_{tot}	Threshold	$Num_{removed}/Num_{total}$
Jun 25, 2020	1.5	1.6	9/22
Jun 27-1, 2020	1.2	1.9	4/22
Sep 12, 2020	1.4	2.1	5/21

S4 Signal of formic acid during the heating

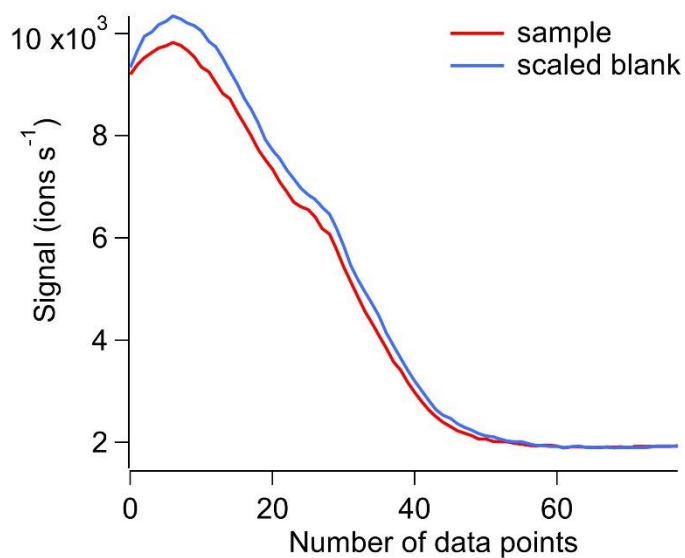


Figure S7: Signal of formic acid (ICH_2O_2^-) during the heating of the sample and the scaled blank, respectively, as a function of heating time. The interval between two data points equals a time period of 30 s. As an example, the signal here is presented from the cloud residual sample on Jun 25, 2020.

S5 Mass spectra of cloud residuals

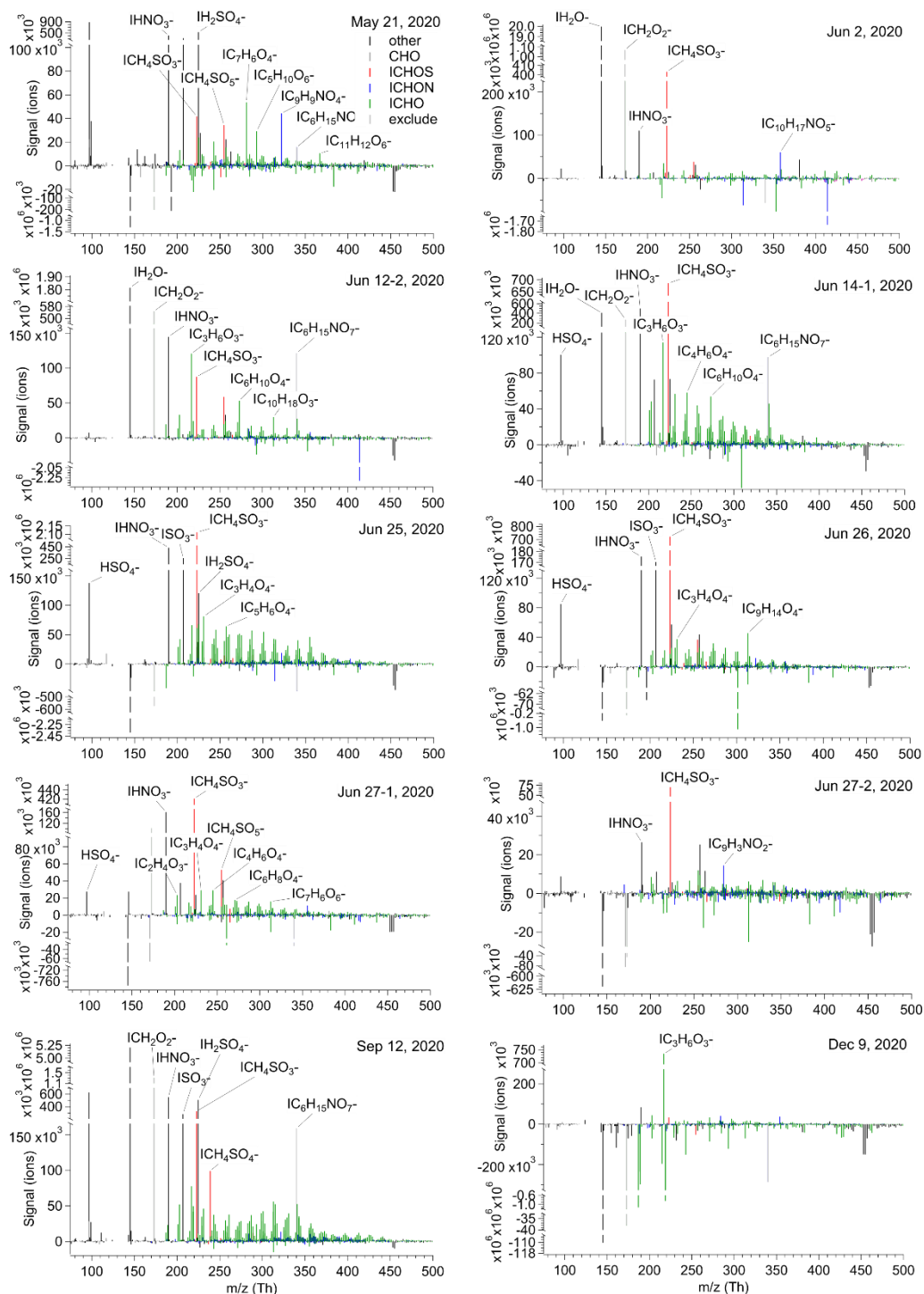


Figure S8: Mass spectra of all cloud residual samples not shown in the main text.

S6 Back trajectories

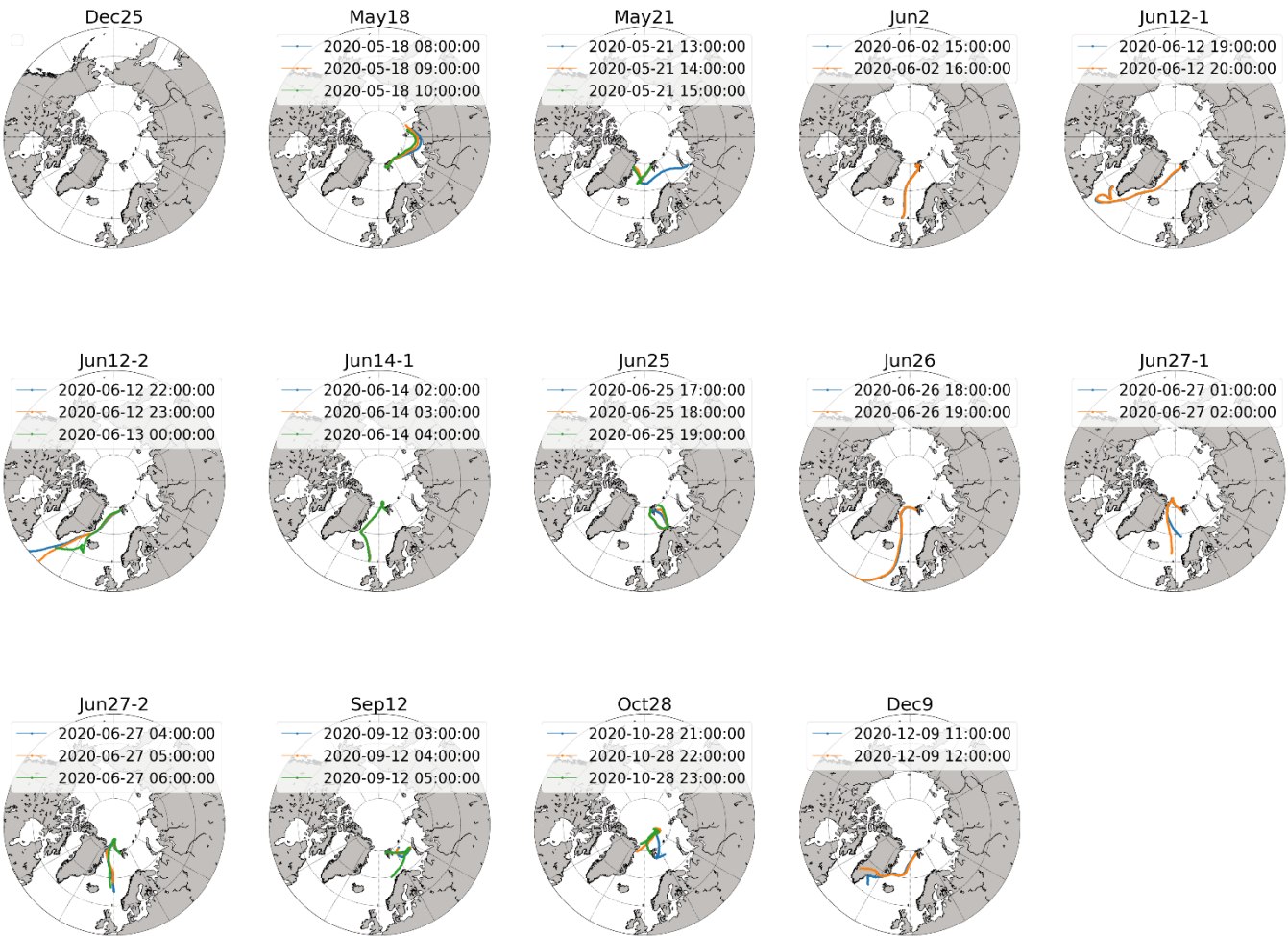


Figure S9: HYSPLIT 5-day back trajectories for the sampling times of all the cloud residual samples.

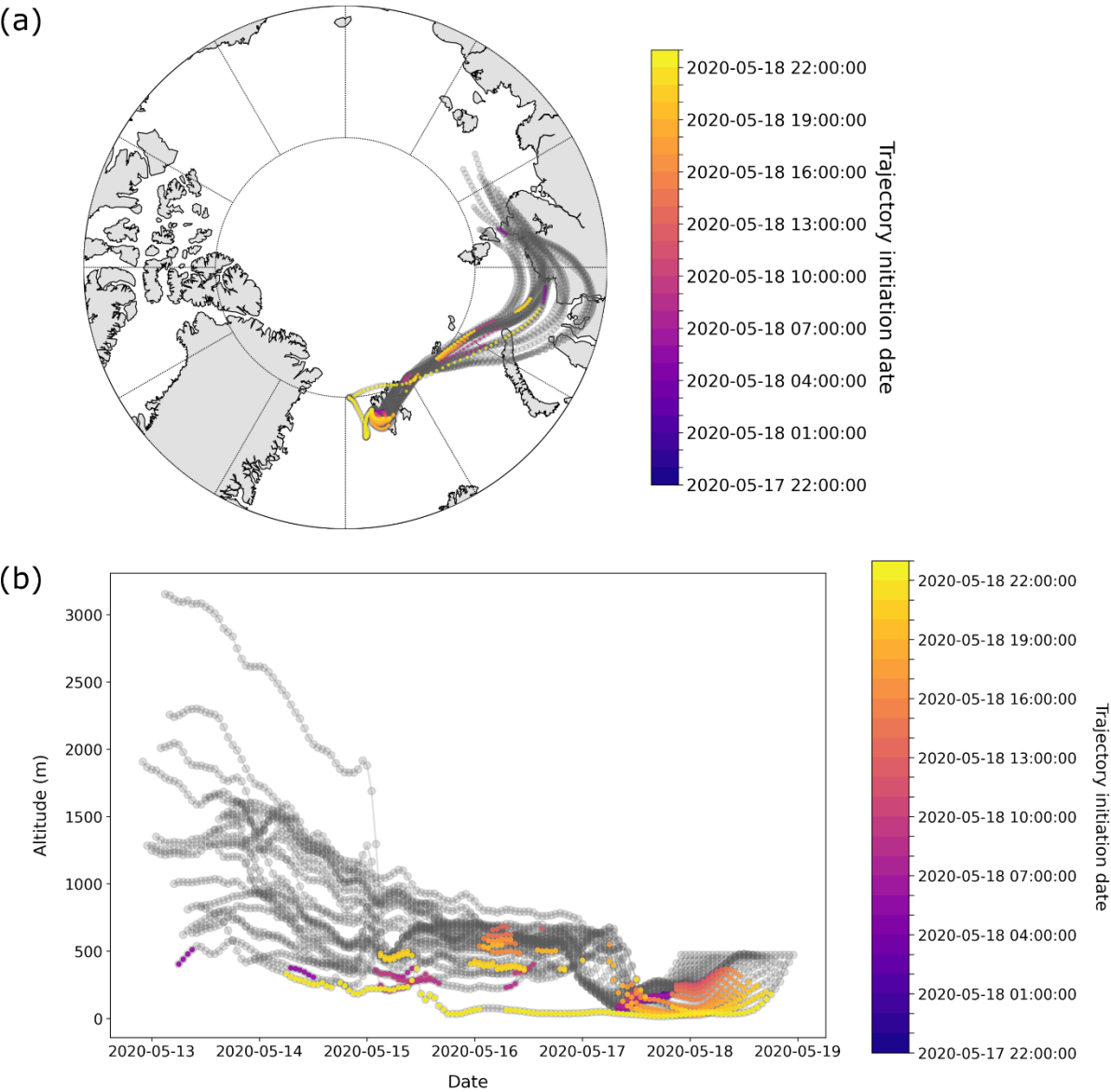


Figure S10: 5 days back trajectories of air masses arriving at the Zeppelin Observatory before, during and after the cloud event color coded by time and height with respect to the boundary layer height (BL). (a) Map view, (b) Trajectory height as a function of time. Grey colors indicate times above the BL, and colors indicate times below the BL.

120

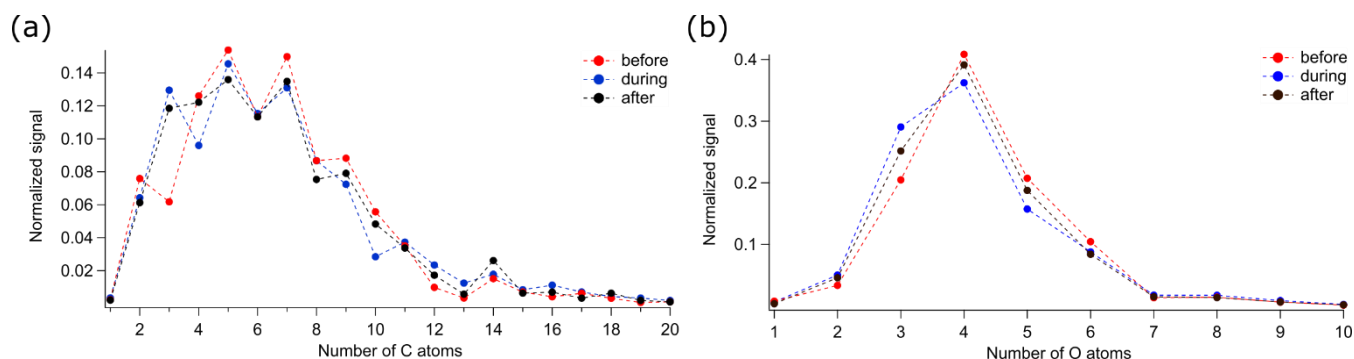


Figure S11: Signal contributions of compounds grouped according to different numbers of (a) carbon and (b) oxygen to the total CHO+CHOI signal for the cloud case May 18, 2020.

S References

Alfarra, M. R., Paulsen, D., Gysel, M., Garforth, A. A., Dommen, J., Prévôt, A. S. H., Worsnop, D. R., Baltensperger, U., and Coe, H.: A mass spectrometric study of secondary organic aerosols formed from the photooxidation of anthropogenic and biogenic precursors in a reaction chamber, *Atmospheric Chem. Phys.*, 6, 5279–5293, <https://doi.org/10.5194/acp-6-5279-2006>, 2006.

Cai, J., Daellenbach, K., Wu, C., Zheng, Y., Zheng, F., Du, W., Haslett, S., Chen, Q., Kulmala, M., and Mohr, C.: Characterization of offline analysis of particulate matter with FIGAERO-CIMS, *Aerosols/Laboratory Measurement/Data Processing and Information Retrieval*, <https://doi.org/10.5194/amt-2022-248>, 2022.

Cloudnet: Classification data from Ny-Ålesund on 12 September 2020, <https://hdl.handle.net/21.12132/1.61025d8bee914c66>, 2021a.

Cloudnet: Classification data from Ny-Ålesund on 25 June 2020, <https://hdl.handle.net/21.12132/1.2068d2269e014b15>, 2021b.

Cloudnet: Classification data from Ny-Ålesund on 27 June 2020, <https://hdl.handle.net/21.12132/1.2068d2269e014b15>, 2021c.

Malloy, Q. G. J., Nakao, S., Qi, L., Austin, R., Stothers, C., Hagino, H., and Cocker, D. R.: Real-Time Aerosol Density Determination Utilizing a Modified Scanning Mobility Particle Sizer—Aerosol Particle Mass Analyzer System, *Aerosol Sci. Technol.*, 43, 673–678, <https://doi.org/10.1080/02786820902832960>, 2009.

McFarquhar, G. M., Ghan, S., Verlinde, J., Korolev, A., Strapp, J. W., Schmid, B., Tomlinson, J. M., Wolde, M., Brooks, S. D., Cziczo, D., Dubey, M. K., Fan, J., Flynn, C., Gultepe, I., Hubbe, J., Gilles, M. K., Laskin, A., Lawson, P., Leaitch, W. R., Liu, P., Liu, X., Lubin, D., Mazzoleni, C., Macdonald, A.-M., Moffet, R. C., Morrison, H., Ovchinnikov, M., Shupe, M. D., Turner, D. D., Xie, S., Zelenyuk, A., Bae, K., Freer, M., and Glen, A.: Indirect and Semi-direct Aerosol Campaign: The Impact of Arctic Aerosols on Clouds, *Bull. Am. Meteorol. Soc.*, 92, 183–201, <https://doi.org/10.1175/2010BAMS2935.1>, 2011.

Verlinde, J., Harrington, J. Y., McFarquhar, G. M., Yannuzzi, V. T., Avramov, A., Greenberg, S., Johnson, N., Zhang, G., Poellot, M. R., Mather, J. H., Turner, D. D., Eloranta, E. W., Zak, B. D., Prenni, A. J., Daniel, J. S., Kok, G. L., Tobin, D. C., Holz, R., Sassen, K., Spangenberg, D., Minnis, P., Tooman, T. P., Ivey, M. D., Richardson, S. J., Bahrmann, C. P., Shupe, M.,

DeMott, P. J., Heymsfield, A. J., and Schofield, R.: The Mixed-Phase Arctic Cloud Experiment, *Bull. Am. Meteorol. Soc.*, 88, 205–222, <https://doi.org/10.1175/BAMS-88-2-205>, 2007.

- 155 Wendisch, M., Macke, A., Ehrlich, A., Lüpkes, C., Mech, M., Chechin, D., Dethloff, K., Velasco, C. B., Bozem, H., Brückner, M., Clemen, H.-C., Crewell, S., Donth, T., Dupuy, R., Ebell, K., Egerer, U., Engelmann, R., Engler, C., Eppers, O., Gehrman, M., Gong, X., Gottschalk, M., Gourbeyre, C., Griesche, H., Hartmann, J., Hartmann, M., Heinold, B., Herber, A., Herrmann, H., Heygster, G., Hoor, P., Jafariserajehlou, S., Jäkel, E., Järvinen, E., Jourdan, O., Kästner, U., Kecorius, S., Knudsen, E. M., Köllner, F., Kretschmar, J., Lelli, L., Leroy, D., Maturilli, M., Mei, L., Mertes, S., Mioche, G., Neuber, R., Nicolaus, M.,
160 Nomokonova, T., Notholt, J., Palm, M., van Pinxteren, M., Quaas, J., Richter, P., Ruiz-Donoso, E., Schäfer, M., Schmieder, K., Schnaiter, M., Schneider, J., Schwarzenböck, A., Seifert, P., Shupe, M. D., Siebert, H., Spreen, G., Stapf, J., Stratmann, F., Vogl, T., Welti, A., Wex, H., Wiedensohler, A., Zanatta, M., and Zeppenfeld, S.: The Arctic Cloud Puzzle: Using ACLOUD/PASCAL Multiplatform Observations to Unravel the Role of Clouds and Aerosol Particles in Arctic Amplification, *Bull. Am. Meteorol. Soc.*, 100, 841–871, <https://doi.org/10.1175/BAMS-D-18-0072.1>, 2019.

165